Journal of Neural Engineering

PAPER • OPEN ACCESS

Far-field electric potentials provide access to the output from the spinal cord from wrist-mounted sensors

To cite this article: Irene Mendez Guerra *et al* 2022 *J. Neural Eng.* **19** 026031

View the article online for updates and enhancements.

You may also like

- Closing the loop between wearable technology and human biology: a new paradigm for steering neuromuscular form and function
Massimo Sartori and Gregory S Sawicki
- A 3D map of the hindlimb motor representation in the lumbar spinal cord in Sprague Dawley rats
Jordan A Borrell, Shawn B Frost, Jeremy Peterson et al.
- Feedforward modulation of gamma motor neuron activity can improve motor command accuracy
Jakob Dideriksen and Francesco Negro

This content was downloaded from IP address 155.198.12.188 on 10/05/2022 at 16:13

Journal of Neural Engineering



OPEN ACCESS

RECEIVED
1 November 2021

REVISED
3 February 2022

ACCEPTED FOR PUBLICATION
18 March 2022

PUBLISHED
5 April 2022

Original content from this work may be used under the terms of the Creative Commons Attribution 4.0 licence.

Any further distribution of this work must maintain attribution to the author(s) and the title of the work, journal citation and DOI.



PAPER

Far-field electric potentials provide access to the output from the spinal cord from wrist-mounted sensors

Irene Mendez Guerra[1], **Deren Y Barsakcioglu**[1], **Ivan Vujaklija**[2], **Daniel Z Wetmore**[3] and **Dario Farina**[1,*]

[1] Department of Bioengineering, Imperial College London, London, United Kingdom
[2] Department of Electrical Engineering and Automation, Aalto University, Espoo, Finland
[3] Reality Labs, Meta, New York, United States of America
[*] Author to whom any correspondence should be addressed.

E-mail: d.farina@imperial.ac.uk

Keywords: neural interface, wrist, far-field potentials, real-time decomposition, motor neurons

Supplementary material for this article is available online

Abstract

Objective. Neural interfaces need to become more unobtrusive and socially acceptable to appeal to general consumers outside rehabilitation settings. *Approach*. We developed a non-invasive neural interface that provides access to spinal motor neuron activities from the wrist, which is the preferred location for a wearable. The interface decodes far-field potentials present at the tendon endings of the forearm muscles using blind source separation. First, we evaluated the reliability of the interface to detect motor neuron firings based on far-field potentials, and thereafter we used the decoded motor neuron activity for the prediction of finger contractions in offline and real-time conditions. *Main results*. The results showed that motor neuron activity decoded from the far-field potentials at the wrist accurately predicted individual and combined finger commands and therefore allowed for highly accurate real-time task classification. *Significance.* These findings demonstrate the feasibility of a non-invasive, neural interface at the wrist for precise real-time control based on the output of the spinal cord.

1. Introduction

In our ever-growing digital world, human-machine interaction has a pivotal role not only in defining our relationship with technology but also in determining its usability and effectiveness. While current input systems such as keyboards or touchscreens are intuitive for most people, their benefits are task-specific (e.g. inputting text or selecting an item). Rising technologies such as virtual or augmented reality offer new capabilities of interaction. To ensure a genuinely immersive experience, the potential of our hands needs to be fully exploited with commands that closely mimic our natural movements in real life. Being able to perform such variety of rich gestures to interact with multiple digital systems intuitively, accurately, and quickly, will revolutionise input technologies. Evermore, bypassing the need of task-specific actuators and developing wearable solutions will make this comprehensive interaction seamless and portable.

In this regard, neural interfaces can be a promising approach to complete this vision. Neural interfaces target the neural code of motor commands to drive external devices in an attempt to provide an intuitive and enhanced interaction with the environment. Although originally developed as a rehabilitation technology, the potential of neural interfaces for large-scale consumer electronics has gained momentum in the past few years. Both applications require high spatiotemporal resolution and population sampling to ensure a representative information bandwidth [1]. Yet, one key difference to appeal general consumers and meet ethical considerations is the need for non-invasive wearable devices [2].

Traditionally, signals from the brain have been leveraged to control prostheses [3], wheelchairs [4], and exoskeletons [5], among other systems [6, 7]. Nonetheless, direct brain interfaces are currently constrained by a trade-off between their information transfer and invasiveness, with non-invasive systems providing substantially smaller information

© 2022 The Author(s). Published by IOP Publishing Ltd

bandwidth than invasive devices [8]. Furthermore, acceptance of brain interfaces for daily use outside rehabilitation applications remains uncertain. In comparison, the peripheral nervous system offers a more accessible window to motor volition [9].

Motor neurons in the spinal cord translate the synaptic inputs they receive from supraspinal centres and peripheral afferents into a neural output sent to their innervated muscle fibres [10]. When the axonal action potentials generated by motor neurons reach the neuromuscular junction, they excite the fibres and produce another potential on the muscle membrane. These muscle fibre action potentials propagate from the end plates in the neuromuscular junction, along the direction of the fibres, to the tendon endings where they terminate.

Electrodes on the skin surface can detect the aggregate activity of muscle fibre action potentials, filtered by the volume conductor [11]. This is the electromyogram signal (EMG), which has been extensively used as input for human-machine interfacing [12]. The most common approach for decoding distal movements of the upper limb is to record EMG from forearm muscles. Still, the most convenient location for long-term adoption of wearable devices is at the wrist due to social acceptance of wristwatches [13, 14]. As forearm muscles converge into the tendons at the wrist, the muscle mass drastically reduces. Interestingly, despite the predominance of non-conductive tendon tissue at the wrist, the muscle-tendon interface shows unique electrical properties.

When muscle fibre action potentials terminate at the tendons, far-field potentials emerge [15]. To understand them, it is necessary to review the electric potential associated to a dipole current source. Briefly, in a dipole (sometimes expressed as $+\ -$), current flows between the positive and negative poles generating a characteristic electric field. Close to the poles, the potential changes rapidly (near-field potential region), while at relatively far distances the effect of the dipole decreases and the potential becomes constant (far-field potential region). In a bounded volume conductor, such as a limb, far-field potentials are non-propagating signal components with fixed amplitude and morphology [16]. A muscle fibre action potential can be modelled as a quadripolar current source travelling along the muscle fibre, comprising two dipoles oriented in opposite directions ($+\ -\ -\ +$), the so-called leading and trailing dipoles [15]. Under this configuration, the far-field potentials of the two dipoles cancel each other and only the stereotypical propagating waveform of the muscle fibre action potential is observed. However, as the dipoles sequentially disappear at the muscle-tendon interface, they only partially cancel each other's far-field potentials, generating a short non-zero net potential.

Far-field potentials have been researched for decades [15–17], but their feasibility as a source of motor control has only been evaluated indirectly. A few studies have recorded EMG signals at the wrist to decode motor intention [18–20]. Using temporal EMG features, Botros *et al* [20] achieved 88% classification accuracy in offline prediction of individual finger tasks and Jiang *et al* [19] obtained 75% in a real-time control task. These accuracies are lower than those generally reported with classic EMG recordings from the forearm [21, 22]. This poorer performance at the wrist has been explained by the convergence of multiple muscle tendons in a reduced space, which results in high crosstalk between the recorded signals.

To compensate for the small detection space in wrist recordings, it would be theoretically possible to decompose EMG signals into the underlying motor neuron activity by reversing the EMG generative model. This problem is often solved by blind source separation [23–27], where the sparseness of the estimated sources is maximised under the assumption that each muscle fibre action potential is unique. This is well-satisfied when recording over the muscle belly (where the propagating muscle fibre action potentials experience their highest amplitudes) with a sufficiently high number of sensors (i.e. in the range of tens to hundreds [28]). However, at the tendons, the propagating components of the muscle fibre action potentials are attenuated, being the far-field potentials the main components of the signals, as discussed above.

Here, we hypothesise that the differences in muscles fibres' conduction velocity, size, position in the volume conductor, and tendon spread would generate unique far-field potentials for each motor neuron, with the same timing (save a constant delay of few ms [29]) as the axonal action potentials from the spinal cord. If this were true, far-field potentials could be extracted from EMG signals recorded over tendon endings, allowing for distal non-invasive neural interfaces (figure 1). To test this hypothesis, we applied blind source separation methods to decompose electrical signals recorded by EMG electrodes and we validated the neural origin of the decomposed signals. Thereafter, we used the neural information obtained from the decomposed signals to predict individual and combined finger presses in offline and real-time conditions. Results showed that the decoded far-field potentials indeed correspond to individual motor neuron discharges, and that this neural decoding enhances the information transfer to accurately predict individual and combined finger commands in offline and real-time control conditions. Therefore, here we present a new high-fidelity, non-invasive, unobtrusive, and socially acceptable neural interface at the wrist as a viable alternative to invasive neural recordings and traditional muscle interfaces.

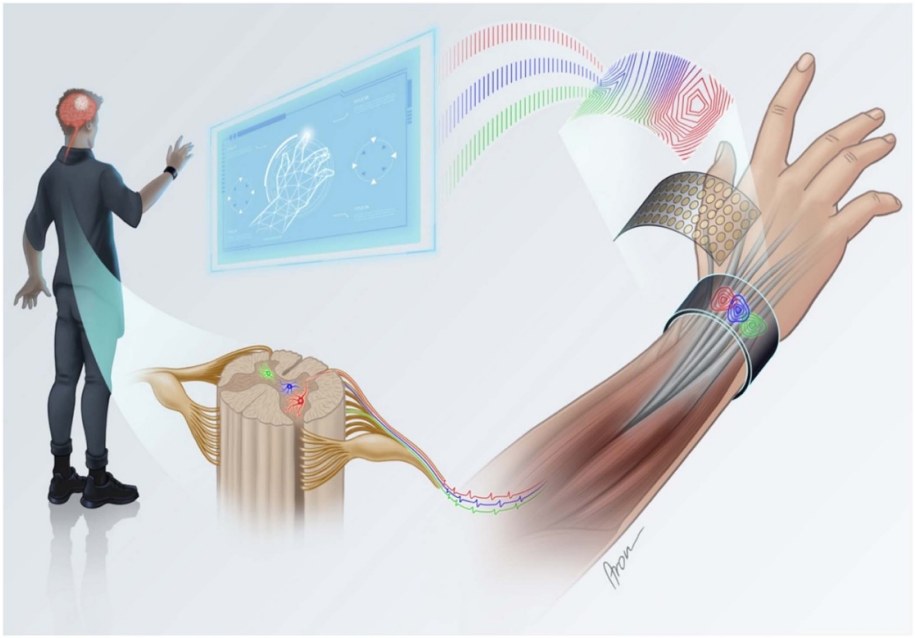


Figure 1. Interfacing motor neurons in the spinal cord non-invasively from the wrist via volume conduction and far-field potentials at the tendon endings. Motor neurons in the spinal cord translate the synaptic inputs they receive from supraspinal centres and peripheral afferents into a neural output sent to the muscles. When excited, they discharge axonal action potentials that reach the neuromuscular junction of the innervated muscle fibres. These muscle fibre action potentials propagate from the end plates to the tendon endings where they terminate generating far-field potentials. These potentials can be detected at the tendon endings of the wrist using electrodes (in this case, arranged in a wristband) due to volume conduction. However, wrist EMG signals experience high crosstalk between each other due to the convergence of multiple tendons in the reduced space of the wrist. To enhance the information transfer needed for precise decoding of motor volition, the generative model of the wrist EMG signals can theoretically be reversed to estimate the activity of the spinal motor neurons as long as the induced far-field potentials at the tendons are unique for each motor neuron.

2. Methods

2.1. Offline experiment

2.1.1. Experimental setup

Nine healthy participants (four females, five males, ages: 23–31) volunteered in the study. Both informed consent forms and experimental protocols were approved by the local ethics committee in accordance with the Declaration of Helsinki.

Two flexible EMG electrode grids (64 channels arranged in 5 × 13 with 8 mm distance, GR08MM1305, OT Bioelettronica) were placed along the circumference of the wrist right below the head of the ulna by visual inspection and physical palpation. The circumference of this channel arrangement was larger than that of the wrist, resulting in overlapping electrodes between the grids. These channels were noted for each subject and discarded in the post-processing steps along with noisy ones. On average, 102 ± 12 channels were kept at the wrist for further analysis. In addition, EMG signals were concurrently recorded from the circumference of the thickest part of the forearm using three electrode grids (64 channels arranged in 8 × 8 with 10 mm distance, GR10MM0808, OT Bioelettronica). Both signals were simultaneously acquired in monopolar mode (reference and ground bands were placed around the elbow) by a multi-channel amplifier (Quattrocento, OT Bioelettronica), bandpass filtered between 10 and 500 Hz, and sampled at 2048 Hz with 16-bit ADC precision. Individual finger flexion forces were recorded concurrently at 10 Hz with five micro load cells (0–5 kg CZL635, Phidget), located in an ergonomic and adjustable platform. The latter was designed to keep the hand supported while in a relaxed position. A custom acquisition framework (Matlab 2019b, The MathWorks, Inc) was implemented to synchronously acquire all the signals.

Participants were seated on a chair with their arm supported and the fingers placed in a comfortable position on top of each force sensor. They were facing a computer screen where cues and visual feedback of their fingers' flexion forces were provided. The maximal voluntary contraction (MVC) level across each finger was calibrated for each participant at the beginning of the experiment. Thereafter, they were instructed to follow the displayed trapezoidal cues (2 s rest, 2 s ramp up, 5 s steady contraction, 2 s ramp down and 2 s rest) at 15% and 30% MVC for each individual finger and the combinations of thumb-index, thumb-middle, index-middle and thumb-index-middle in a randomized order (18 trials in total).

After acquisition, EMG signals were digitally bandpass filtered between 20 and 500 Hz (Butterworth).

2.1.2. Decomposition of far-field potentials

Far-field potentials were extracted from wrist EMG signals using convolutive blind source separation. Although the EMG generative model [30] and the convolutive blind source separation algorithm [26] have been extensively described before, here we provide a brief description highlighting the differences between recordings at muscle belly and over the tendons at the wrist.

Generally, at the muscle belly, EMG signals constitute the sum of the underlying muscle fibre action potentials. The latter can be modelled as the convolution of a series of delta trains (representing the motor neurons' firings) and the corresponding potential affected by the volume conductor. However, at the wrist, the propagating components of the muscle fibre potential are attenuated, far-field potentials being the main signal source. Furthermore, most muscle belly recordings target a specific muscle. In contrast, at the wrist, most muscle fibres converge into a series of densely packed tendons, and therefore the recorded potentials are generated by multiple pools of spinal motor neurons.

Given the above description of the origin of electric signals at the tendon regions, the following mathematical model holds:

$$\boldsymbol{x}(k) = \sum_{p=1}^{P} \sum_{l=0}^{L-1} \boldsymbol{H}_{\mathrm{p}}(l)\, \boldsymbol{s}_{\mathrm{p}}(k-l) + \boldsymbol{n}(k) \qquad (1)$$

where $\boldsymbol{x}(k)$ are the wrist EMG signals at time k generated by the additive contributions of P spinal motor neuron pools innervating different muscles, with additive independent noise $\boldsymbol{n}(k)$. In equation (1), $\boldsymbol{s}_{\mathrm{p}}$ represents the sets of delta trains in the pth motor neuron pool, convolved by their corresponding far-field potentials over their length L.

The high-frequency nature of the far-field components at the tendons corresponds to short temporal durations compared to the propagating muscle fibre action potentials [31, 32], which translates in relatively low values for L. In this way, the far-field potentials ($\boldsymbol{H}$) are a better approximation of the source delta functions than the muscle fibre action potentials. This property equivalently implies greater temporal sparseness for the train of action potentials of each source.

To solve the inverse problem in a tractable way, the matrices of the far-field potentials ($\boldsymbol{H}_{\mathrm{p}}$) and motor neurons' firings ($\boldsymbol{s}_{\mathrm{p}}$) are rewritten appending their delayed versions along L to compensate for the effect of the convolution. Moreover, wrist EMG signals ($\boldsymbol{x}(k)$) are also extended to an artificial delay proportional to L and inversely proportional to the number of electrodes to offset the increase of motor neurons to estimate. This yields the following equation:

$$\tilde{\boldsymbol{x}}(k) = \sum_{p=1}^{P} \tilde{\boldsymbol{H}}_{\mathrm{p}} \tilde{\boldsymbol{s}}_{\mathrm{p}}(k) + \tilde{\boldsymbol{n}}(k) \qquad (2)$$

where $\tilde{}$ indicates the extended variables. Equation (2) reflects the presence of multiple spinal motor neuron pools innervating different muscles due to the convergence of their tendon endings at the wrist. Nevertheless, their estimation can be conveniently carried out in a single matrix form by concatenating the contributions of each pool to the global far-field potentials ($\widetilde{\widetilde{\boldsymbol{H}}}$) and motor neuron firings ($\widetilde{\widetilde{\boldsymbol{s}}}$) as follows:

$$\widetilde{\widetilde{\boldsymbol{H}}} = \left[\widetilde{\boldsymbol{H}}_1,\ \widetilde{\boldsymbol{H}}_2, \cdots, \widetilde{\boldsymbol{H}}_{\mathrm{P}}\right] \qquad (3)$$

$$\widetilde{\widetilde{\boldsymbol{s}}}(k) = \left[\widetilde{\boldsymbol{s}}_1(k), \widetilde{\boldsymbol{s}}_2(k), \cdots, \widetilde{\boldsymbol{s}}_{\mathrm{P}}(k)\right]^{\mathrm{T}}. \qquad (4)$$

Such that:

$$\widetilde{\widetilde{\boldsymbol{x}}}(k) = \widetilde{\widetilde{\boldsymbol{H}}}\, \widetilde{\widetilde{\boldsymbol{s}}}(k) + \widetilde{\widetilde{\boldsymbol{n}}}(k). \qquad (5)$$

If the noise component is considered negligible, this expression can be rewritten into:

$$\widetilde{\widetilde{s}}(k) = \boldsymbol{B}\widetilde{\widetilde{\boldsymbol{x}}}(k) \qquad (6)$$

where $\boldsymbol{B}$ are the decomposition filters that approximate the pseudo-inverse of $\widetilde{\widetilde{\boldsymbol{H}}}$. The matrix $\boldsymbol{B}$ can be computed using blind source separation by maximising the sparseness of the sources, as long as the far-field potential generated by each motor neuron is unique in relation to the far-field potentials associated to other motor neurons at their corresponding tendon endings. This condition has been extensively validated for the propagating components of the muscle fibre action potentials [33–36], but it has never been tested for the far-field components generated at the tendon endings. Therefore, this assumption needed to be confirmed experimentally.

To validate it, the convolutive blind source separation [26] algorithm was used to invert the far-field potentials of the model and decode the motor neuron firings from the recorded wrist EMG signals. The algorithm assumes there are more observations (wrist EMG signals) than sources (firing motor neurons), and that the latter are sparse (see [26, 30] for details). In addition, the decomposition filters (inverse of the far-field potentials) are considered to be causal and to have a finite-length impulse response. Briefly, convolutive blind source separation applies an initial whitening and fast fixed-point algorithm [37, 38] that iteratively maximises sparseness of the sources using:

$$\boldsymbol{b}_{i+1} = E\left\{\boldsymbol{z}\, g'\left(\boldsymbol{b}_i^T \boldsymbol{z}\right)\right\} - E\left\{g''\left(\boldsymbol{b}_i^T \boldsymbol{z}\right)\right\} \boldsymbol{b}_i \qquad (7)$$

where i represents the iteration number, $\boldsymbol{z}$ are the whitened wrist EMG signals, and $g'$and g'' are the first and second derivatives of the sparsity contrast function $G(x) = x^2/2$. In each iteration, $\boldsymbol{b}$ undergoes orthogonalisation and normalisation to avoid repeated and trivial sources [26]. This step is followed by a peak-detection and clustering to identify

their corresponding discharge timings in the estimated delta trains [26]. After this process, only the original motor neuron firings (non-delayed versions) were kept for the rest of the analyses.

For the offline analysis only, the output of this fully automatic decomposition was checked in a semi-supervised approach that enables the modification of the thresholds of the local peak detection algorithm to update the filters of poorly detected sources and recalculate the motor neuron firings [39]. Repeatedly detected motor neurons within each contraction (with >30% shared spike timings [40]) were removed at this stage.

2.1.3. Physiological analysis

The decomposition output was evaluated in terms of the number of identified motor neurons at the wrist and the percentage of those that corresponded to muscle fibre potentials occurring concurrently at the forearm. To do so, the fibre potentials at the forearm were calculated by spike-triggered averaging the forearm signals in 50 ms windows using the discharge times identified from the wrist as triggers. The average muscle fibre potentials obtained in this way were considered detectable if their peak amplitude was higher than four times the baseline noise [41]—computed as the standard deviation over the first and last 15 ms of the spike triggered average. If one or more channels in the array met this condition, it was concluded that the corresponding source identified from the wrist corresponded to the activation of muscle fibre action potentials and thus to the discharges of a spinal motor neuron.

The accuracy of the decoding was further assessed based on the pulse-to-noise ratio (PNR) of the estimated spike train (mean of the detected spiking activity divided by the mean baseline of the estimated source expressed in dB [42]). In addition, the coefficient of variation of the inter spike intervals (ratio between the standard deviation and mean of the inter spike intervals expressed as a percentage) and motor neurons' discharge rate (ratio between the number of action potentials fired by a motor neuron and their active period measured in seconds) were computed to evaluate their physiological properties.

2.1.4. Finger command classification

For the control analysis, motor neurons across contractions were tracked based on the 2D correlation coefficient between their far-field potential maps. These maps were calculated by spike-triggered averaging over 25 ms windows all the wrist EMG signals from the electrode array, centred at the timings of the motor neurons' spikes [43]. The analysis was carried out only for those channels with significant peak amplitude (i.e. higher than two times the standard deviation of that motor neuron's peak amplitudes among all channels). Motor neurons were considered the same if their normalised cross-correlation coefficient exceeded 0.70 [44].

Thereafter, the steady contraction part (5 s) of each finger flexion was selected and concatenated along with 5 s of rest for feature extraction. Motor neurons' firings were windowed in intervals of 120 ms with 40 ms step to compute the spike count of each motor neuron. Wrist EMG signals were windowed alike to extract four time-domain features [45] (root mean square, slope sign changes, zero crossings and waveform length) for each channel. Although multiple features have been proposed to decode movement intentions from electric signals [20], the selected feature set is the most common in pattern recognition tasks [46].

A multilayer perceptron with one hidden layer and ten hidden neurons [47] was used to classify the wrist EMG and decoded motor neuron features separately into ten classes (nine finger flexions plus rest). The multilayer perceptron was trained using the gradient descent with momentum and adaptive learning rate backpropagation algorithm. Performance was evaluated in terms of classification accuracy applying ten-fold cross-validation. In addition, classification accuracy was calculated for two scenarios: training and testing with contractions from one force level only, and from both levels combined. In both cases, 2 s of each class were used for training and the remaining data (3 s for the single force dataset, and 8 s for the combined) for testing.

In a preliminary evaluation, principal component analysis (PCA) was applied to reduce the dimensionality of the motor neurons and wrist EMG feature sets preserving 95% of their variance. However, this did not increase the performance based on motor neuron decoding while it significantly decreased the classification accuracy of wrist EMG features (<60%) with respect to the baseline (no PCA), in all scenarios. For this reason, no dimensionality reduction was applied in further analyses.

2.1.5. Statistical analyses

Statistical analyses were carried out to assess the effect of force levels, finger contractions, and data type (wrist EMG vs motor neurons) in the physiological and task classification metrics. Statistical significance was set to $p < 0.05$. If two factors were involved, a two-way repeated measures analysis of variance (ANOVA) was performed. Normal distribution of the data was determined by the Shapiro-Wilk test of normality. Few exceptions were found in (a) the number of motor neurons in the little finger at 15% MVC ($p = 0.019$), (b) the PNR of the thumb at 15% ($p = 0.037$) and index at 30% ($p = 0.005$), and (c) coefficient of variation of the little at 15% ($p = 0.006$), thumb-index at 15% ($p = 0.029$) and thumb at 30% ($p = 0.001$). However, this low proportion of non-normal levels was considered acceptable

for the two-way repeated measures ANOVA. The assumption of sphericity was checked by Mauchley's test and if not satisfied, the Greenhouse-Geisser correction was applied to the degrees of freedom. If two-way interaction between the factors was found, the simple main effects were analysed with focused one-way repeated measures ANOVA fixing the levels of the interacting factors.

Otherwise, the main effects were analysed by one-way repeated measures ANOVAs over the pooled data. Bonferroni correction was applied for pair-wise comparisons. When only one factor was involved, one-way repeated measures ANOVA was carried out. All statistical analyses were performed in IBM SPSS Statistics 26.

2.2. Real-time experiment

Four healthy participants (two females, two males, ages: 25–32) participated in the online experiment (approved by the local ethics committee in accordance with the Declaration of Helsinki) after signing informed consent forms.

In this case, only wrist EMG signals from the wrist were acquired following the same setup previously described. Participants were comfortably seated in front of a computer screen, with their right hand resting in a neutral position on top of a table. During training, they were asked to perform isometric finger contractions against the table at up to a comfortable level following trapezoidal cues (2 s rest, 2 s ramp up, 5 s steady contraction, 2 s ramp down and 2 s rest). Three repetitions each individual finger, the combinations of thumb-index, thumb-middle, index-middle, and thumb-index-middle, as well as rest, were recorded in a randomised order (30 trials in total).

To extract motor neurons' firings in real-time, we implemented a dual phase blind source separation [27]. In the first calibrating phase, the algorithm followed the same procedure described above to identify the latent motor neurons firings by compensating the far-field potentials. Then, the obtained inverse of the far-field potential filters was applied to new wrist EMG signals epochs to decompose the activity of the previously identified motor neurons, and detect new far-field potentials using the stored spike and noise centroids of each source [27]. In this case the training set was used to calibrate the decomposition parameters for its later implementation in real-time during the control task. The algorithm was incorporated into the previously described acquisition framework (Matlab 2019b, The MathWorks, Inc) with a system update rate of 40 ms for processing, and visualization. After calibration, the identification of new firings took an average of 2.6 $\pm$ 0.4 ms for 128 wrist EMG signals in batches of 64 samples per channel (equivalent to 31.2 ms acquisition latency), as computed on an Intel Core i7 2.8 GHz, 16 GB RAM. This still allowed 37.4 ms for further processing, such as for feature extraction, classification, and visualization. Therefore, the maximum latency for acquisition and processing of the overall system was 71.2 ms, well below the 100 ms optimal delay in myoelectric control [48].

To maximise the number of detected neurons, each contraction was decomposed separately during calibration. Thereafter, those motor neurons with more than 20% of shared spikes were considered equal and only the one with highest PNR was preserved to avoid redundant activity. As in the previous experiment, the spike count of each motor neuron was calculated over sliding windows of 120 ms with 40 ms step (coinciding with the update rate of the system). On the other hand, the root mean square, slope sign changes, zero crossings and waveform length were extracted for the wrist EMG signals using the same windowing process.

Two multilayer perceptrons with one hidden layer and ten hidden neurons [47] were used to classify the motor neurons firings and wrist EMG features separately into ten classes (nine finger flexions and rest). They were trained using gradient descent with momentum and adaptive learning rate backpropagation over the steady part of the contraction. Both multilayer perceptrons were tested separately in a real-time task with four targets of each class (40 targets in total). Participants were given 5 s to attempt each target, with a required hold time of 500 ms to consider the target successfully reached. Performance was measured in terms of completion rate (number of successful targets divided by the total number of targets, expressed as a percentage) and completion time (time needed to successfully achieve a target).

3. Results

To validate the wrist neural interface, we investigated the physiological properties of the decoded far-field potentials, and then assessed their performance in offline and real-time prediction of finger tasks.

3.1. Physiological analysis

Figures 2(a) and (b) show the EMG acquisition setup at the wrist with the individual finger forces, and the cues to the subjects. Wrist EMG signals were decomposed into a series of discharge timings (decoded wrist EMG signals) by convolutive blind source separation. A representative contraction with the force profile, wrist EMG signal, and the corresponding decoded activity are depicted in figure 2(c). Once the wrist EMG signals have been decomposed, the spatial representation of the far-field potentials can be recovered by spike-triggered averaging the wrist EMG signals over time intervals centred at the detected discharge times. Figure 2(d) shows representative 2D amplitude maps of wrist EMG signals and

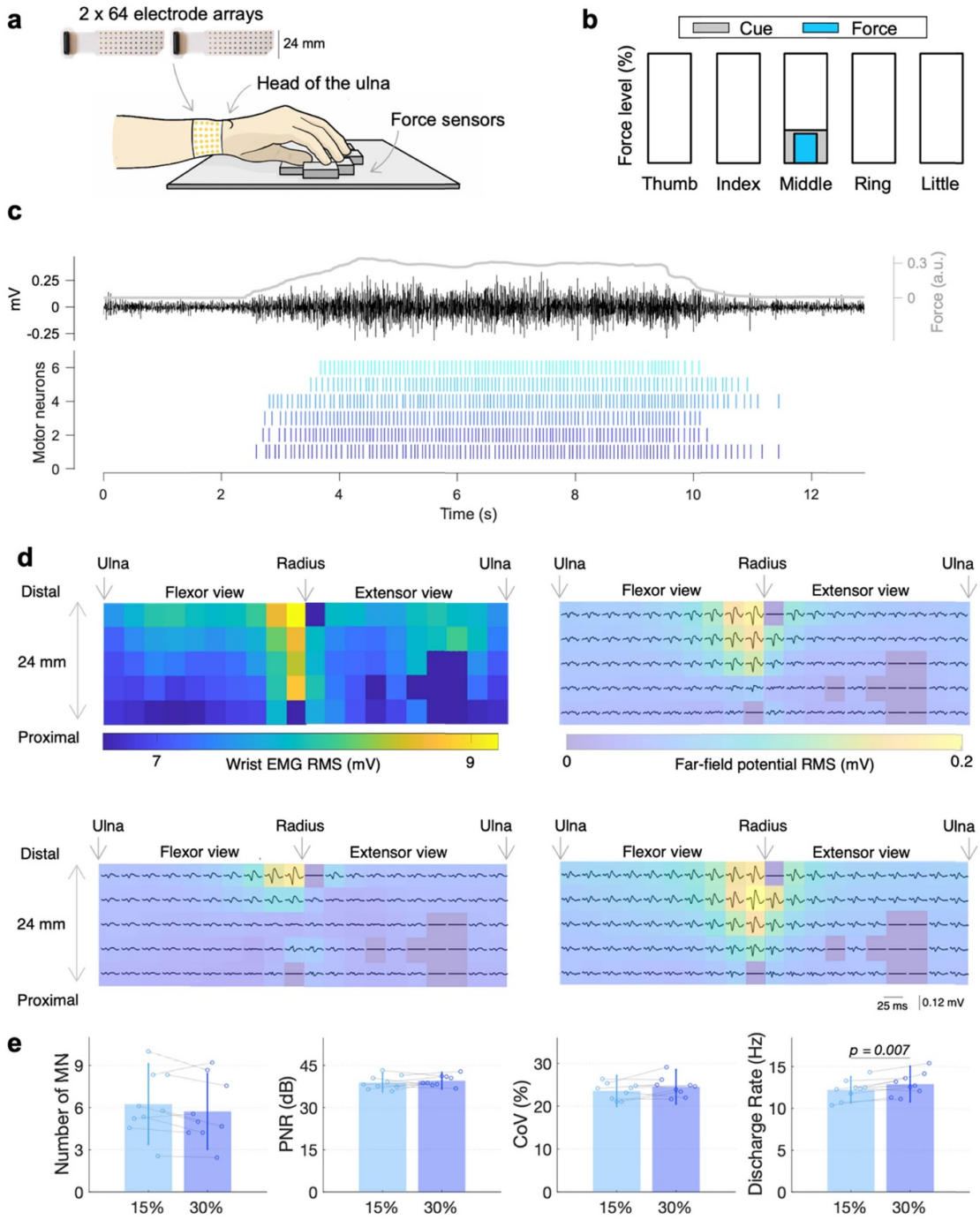


Figure 2. Decoded far-field potentials from the wrist interface. (a) Experimental setup for the concurrent acquisition of the wrist EMG signals and individual finger flexion forces. (b) Participant's visual feedback with the contraction cues in grey and the exerted forces in blue. (c) A representative contraction from one participant with the force profile in grey, one wrist EMG signal in black, and the decomposed spike trains (motor neuron firings). (d) (top left) 2D spatial distribution of the root mean square (RMS) of each channel of the wrist EMG signals from one representative contraction, (top right and bottom) three examples of the reconstructed far-field potentials of three decoded motor neurons from the same contraction after spike-triggered averaging along with their corresponding RMS spatial maps. The channels in dark blue were discarded due to noise interference. (e) Physiological analysis of the decoded motor neurons' firings from the wrist for 15% (light blue) and 30% (dark blue) force efforts in terms of the number of detected motor neurons (MN), pulse-to-noise ratio (PNR), coefficient of variation (CoV) of the inter spike intervals, and motor neuron discharge rate averaged across finger movements and subjects. The results indicate that the decoded far-field potentials from the wrist are accurate (PNR > 30 dB and CoV < 30%) and comply with motor neuron's physiological behaviour (DR between 5 and 25 Hz). The reported significance levels are based on two-way repeated measures ANOVA.

three examples of the far-field potentials associated to single motor neurons. The distributions of electric potentials recovered from the wrist are unique for each motor neuron, with high synchronisation in their peak amplitude times within neurons due to the far-field nature of these electrical activities.

On average, 6 ± 3 motor neurons were identified per finger contraction at each force level. To ensure

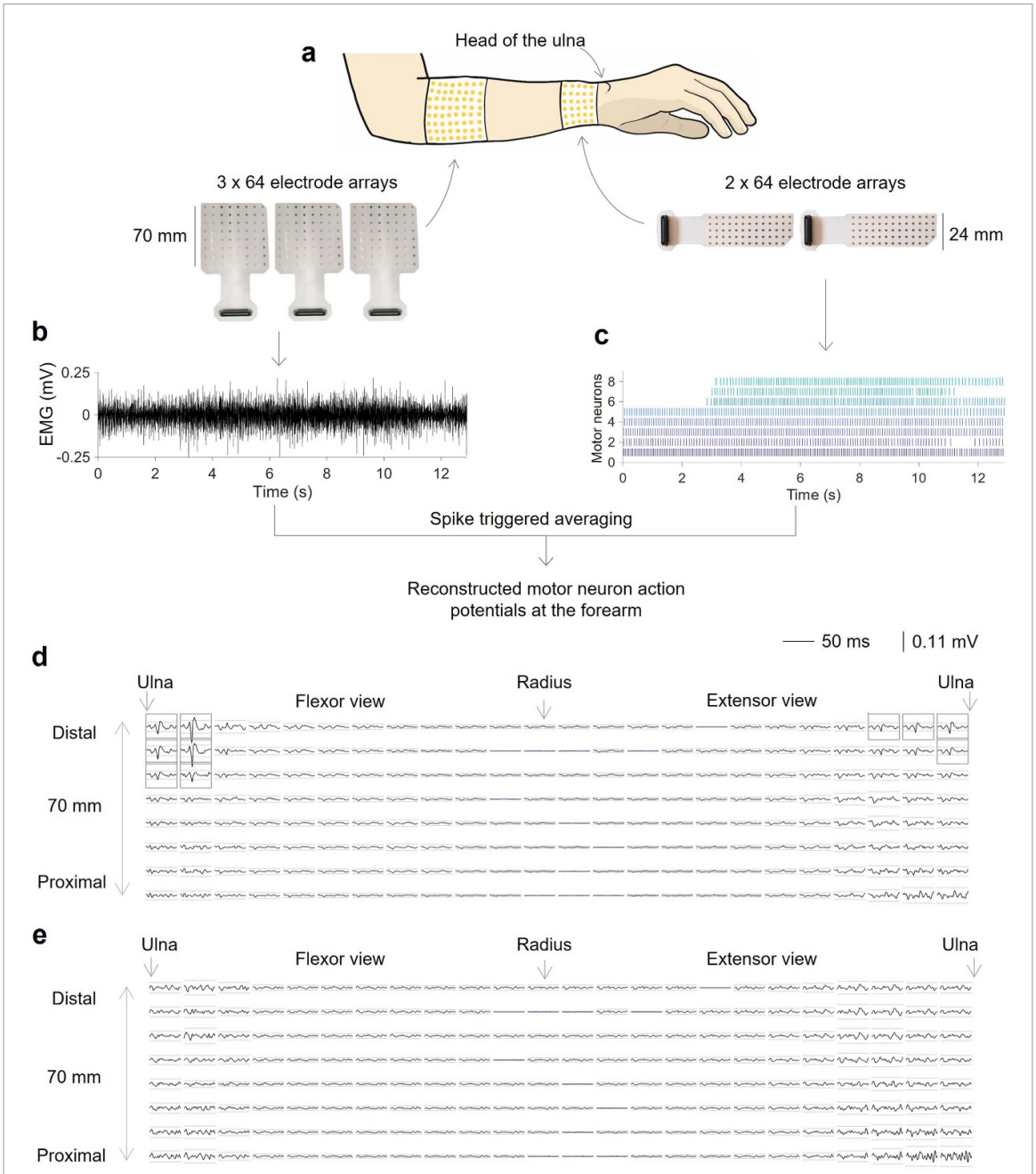


Figure 3. Retracing muscle fibre action potentials at the forearm from the far-field potentials decoded at the wrist via spike triggered averaging. This analysis showed that 703 out of 970 far-field potentials decoded from the wrist were retraceable to the forearm, which supports the neural origin of the decoded far-field potentials. (a) Acquisition setup for concurrent recording of EMG signals at the forearm and the wrist. (b) Representative EMG signal from a single contraction at the forearm. (c) Decoded motor neuron discharge timings from the far-field potentials at the wrist for the same contraction. (d) Representative example of a reconstructed muscle fibre action potentials at the forearm from the far-field potentials at the wrist after spike trigger averaging. Grey boxes indicate those channels whose peak amplitude exceeded four times the baseline (calculated as the standard deviation of the first and last 15 ms). (e) Representative example of a spike triggered average that yielded in no retraceable muscle fibre action potential.

that this decomposed activity indeed represented the neural output from the spinal cord, the discharge timings of the decoded wrist EMG signals were used to trigger an average of the EMG signals concurrently recorded at the forearm (figure 3). The rationale for this processing is that if the discharge times decoded at the wrist correspond to the times of activation of spinal motor neurons, then the triggered average should identify muscle fibre potentials at the forearm above the baseline noise. Indeed, motor neuron activity determines muscle fibre activity synchronous with the motor neuron firings. Therefore, if the decoded times of activation from the wrist determine action potentials of muscle fibres at the forearm when used as triggers, they must correspond to discharge patterns of motor neurons. This approach provided a means for robustly validating the wrist neural interface. The action potentials at the forearm obtained

by spike-triggered average were considered above the baseline noise if their peak amplitude was greater than four times the noise level, as commonly assumed in spike sorting [41] (figure 3). From the total population of 970 detected motor neurons at the wrist, 703 (72.47%) resulted in detectable action potentials at the forearm. This is an extremely high proportion, considering that motor neurons detected at the wrist may innervate muscle fibres deep into the muscle which therefore would not produce sufficiently large action potentials at the forearm skin surface. This result indicated that the timings of activation of the decoded far-field potentials indeed correspond to neural activity from the output layer of the spinal cord. This demonstrates that a peripheral recording from the skin overlying tendon tissue can be decoded into the ultimate neural code of movement.

We then used the PNR to assess the quality of the decoded motor neuron firings. At both force levels, the PNR was greater than 30 dB and generally higher than usually observed when decoding classic EMG recordings from the forearm [36, 49–51] (38.9 ± 2.3 dB and 39.6 ± 3.0 dB for 15% and 30% MVC, respectively) (figure 2(e)). These levels of PNR correspond to an accuracy in detection of spikes in the estimated sources with >90% sensitivity and <2% false alarm rate [42].

After validating the decoding procedures, we further analysed the properties of the decoded discharge patterns to verify whether they were consistent with known physiological properties. We extracted the average discharge rate of each identified motor neuron as well as the coefficient of variation of the estimated inter-spike intervals. The estimated motor neuron discharge rates were within the physiological range of 5–25 Hz [52, 53] at both force levels (12.23 ± 1.58 Hz and 12.90 ± 2.14 Hz at 15% and 30% MVC, respectively) (figure 2(e)), being significantly higher at 30% than at 15% MVC ($F_{1,8} = 12.879$, $p = 0.007$, one-way repeated measures ANOVA), in agreement with motor neuron's rate coding in force production [54]. The coefficient of variation of the estimated inter spike intervals was 23.51 ± 3.63% and 24.47 ± 4.01%, for 15% and 30% MVC, respectively (figure 2(e)), which is within known physiological values [40].

The analysis of accuracy via spike-triggered average and PNR, as well as the physiological analysis of motor neuron behaviour demonstrated the validity and accuracy of the proposed decoding technique. Overall, these results show the accurate identification of the activity of individual spinal motor neurons through non-invasive recordings overlying the tendon endings at the wrist. After confirming the validity and accuracy, we established a human-machine interface based on the proposed neural decoding approach.

3.2. Finger command prediction (offline)

The decoded motor neuron activity was used to classify the corresponding finger command (individual and combined finger contractions plus rest, 10 classes in total) for each force effort separately and when contractions from both force efforts were combined into a single dataset. As a reference, we compared the classification from motor neurons with that obtained using the wrist EMG signals. Figure 4(a) shows the resulting finger classification accuracy. Statistically significant two-way interaction was found between force levels and data type ($F_{1,8} = 13.807$, $p = 0.006$; two-way repeated measures ANOVA), so the simple main effects were analysed. When the two force levels were used independently, the decoded motor neurons yielded in significantly higher finger classification accuracy than wrist EMG signals at both 15% (96.93 ± 2.09% vs 81.23 ± 10.04 %; $F_{1,8} = 23.379$, $p = 0.001$, one-way repeated measures ANOVA) and 30% MVC (97.60 ± 1.75% vs 85.62 ± 6.86 %; $F_{1,8} = 31.036$, $p = 0.00$, one-way repeated measures ANOVA). In addition, the effect of force was only significant for the wrist EMG signals, yielding in higher classification accuracy at the highest force effort ($F_{1,8} = 8.026$, $p = 0.022$, one-way repeated measures ANOVA).

To simulate more realistic control conditions with variable force levels, the classification accuracy was also calculated after training and testing with finger contractions from both force levels combined. Figure 4(b) shows how both force efforts were combined into the training and testing sets for each class during cross-validation. The gain in finger classification accuracy when decoding the motor neuron firings from the far-field potentials was even greater in this condition (95.65 ± 2.76% vs 69.04 ± 10.61% for motor neurons and wrist EMG signals, $F_{1,8} = 64.606$, $p < 0.001$, one-way repeated measures ANOVA).

Figure 4(c) depicts the confusion matrices averaged across all subjects for the individual and combined force conditions, for both wrist EMG signals (top) and the decoded motor neuron firings (bottom).

Overall, the motor neuron activation patterns identified from the wrist provided a highly accurate prediction of finger commands.

3.3. Real-time control

Finally, the proposed neural interface was implemented in real-time following the processing pipeline depicted in figure 5(a). A representative example of the decoded motor firings after calibrating the neural interface is shown in figure 5(b). On average, 78 ± 8 motor neurons were identified across all tasks for each participant. During the online tests, four targets per class (ten classes including individual and combined finger contractions plus rest, resulting in 40 targets in

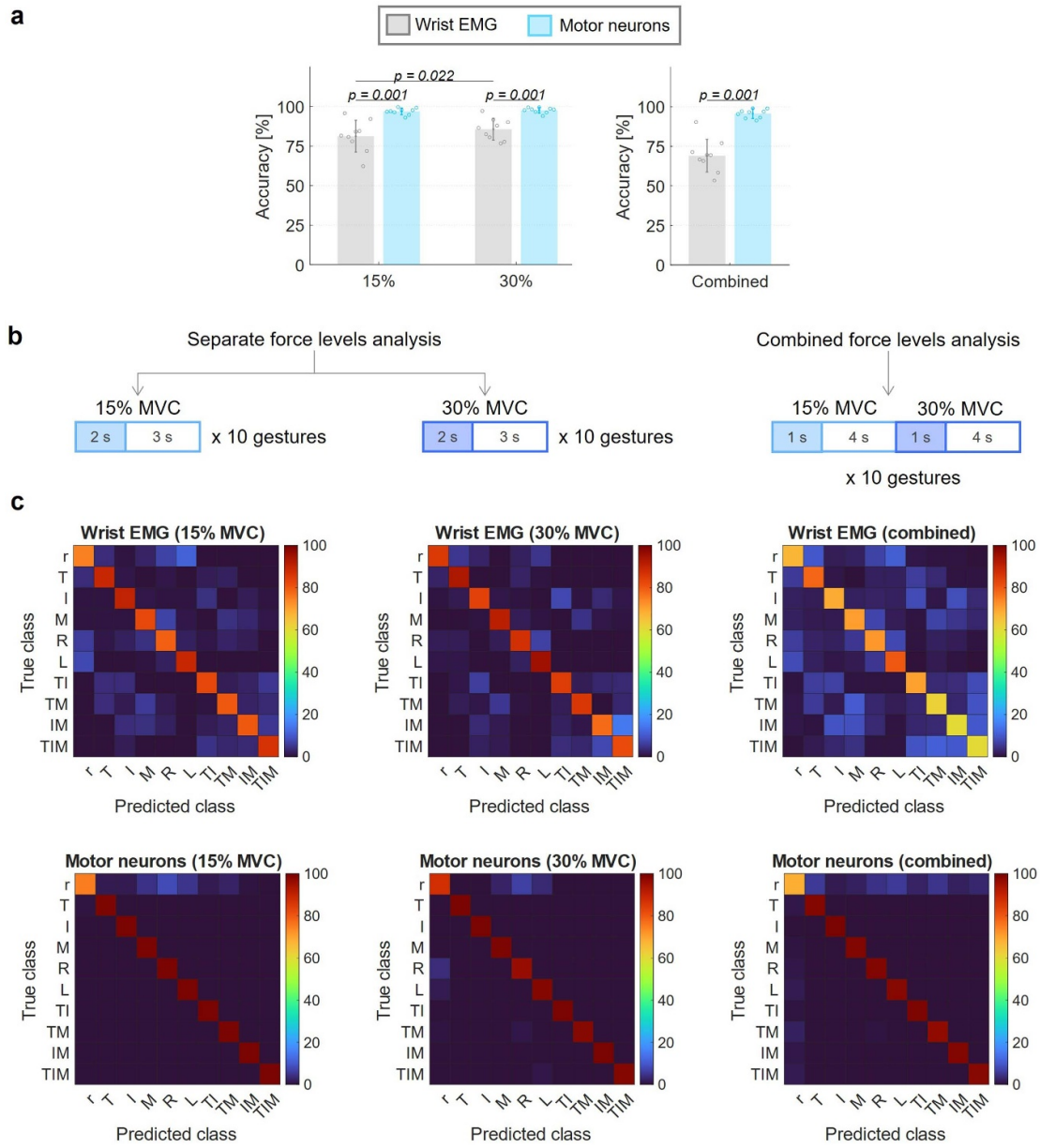


Figure 4. Offline finger classification performance. (a) Mean finger classification accuracy (nine finger flexions plus rest, ten classes in total) for the wrist EMG signals (in grey) and decoded motor neurons' firings from the wrist (in blue) from each force effort (separate analysis) and when both were combined into a single dataset. Plot significances are based on two-way (left) and one-way (right) repeated measures ANOVAs. (b) Blocks representing the ratio between training (shaded) and testing (clear) sets for each class during the ten-fold cross-validation. (c) Confusion matrices with the overall classification accuracy (colour-coded) for each class (r: rest, T: thumb, I: index, M: middle, R: ring, L: little, TI: thumb-index, TM: thumb-middle, IM: index-middle, and TIM: thumb-index-middle) for wrist EMG signals (top) and the decoded motor neurons (bottom) in each force condition. The obtained classification accuracies show that the decoded motor neuron activity is a better predictor of underlying finger flexion than the wrist EMG signals, with high accuracy (high diagonal components in (c) with few off-diagonal elements), irrespective of the force level.

total) were presented to the participants in randomized order. The participants were given 5 s to attempt each target with a success condition of maintaining the correct gesture for 500 ms (figure 5(c)). The mean completion rate resulted significantly higher for the motor neuron (93.12 ± 2.39 %) than for the wrist EMG signals (56.87 ± 18.41%), while maintaining similar completion times (1.81 ± 0.89 s vs 1.65 ± 0.82 s).

The poor online control capacity when using wrist EMG signals without neural decoding is in agreement with previous work [19]. Conversely, the control using separated motor neuron activation patterns was extremely accurate and provided large information transfer (ten classes, ∼93% successful task completions).

4. Discussion

We have shown that the neural information sent from the spinal cord to muscles can be accurately decoded at the single motor neuron level from the far-field

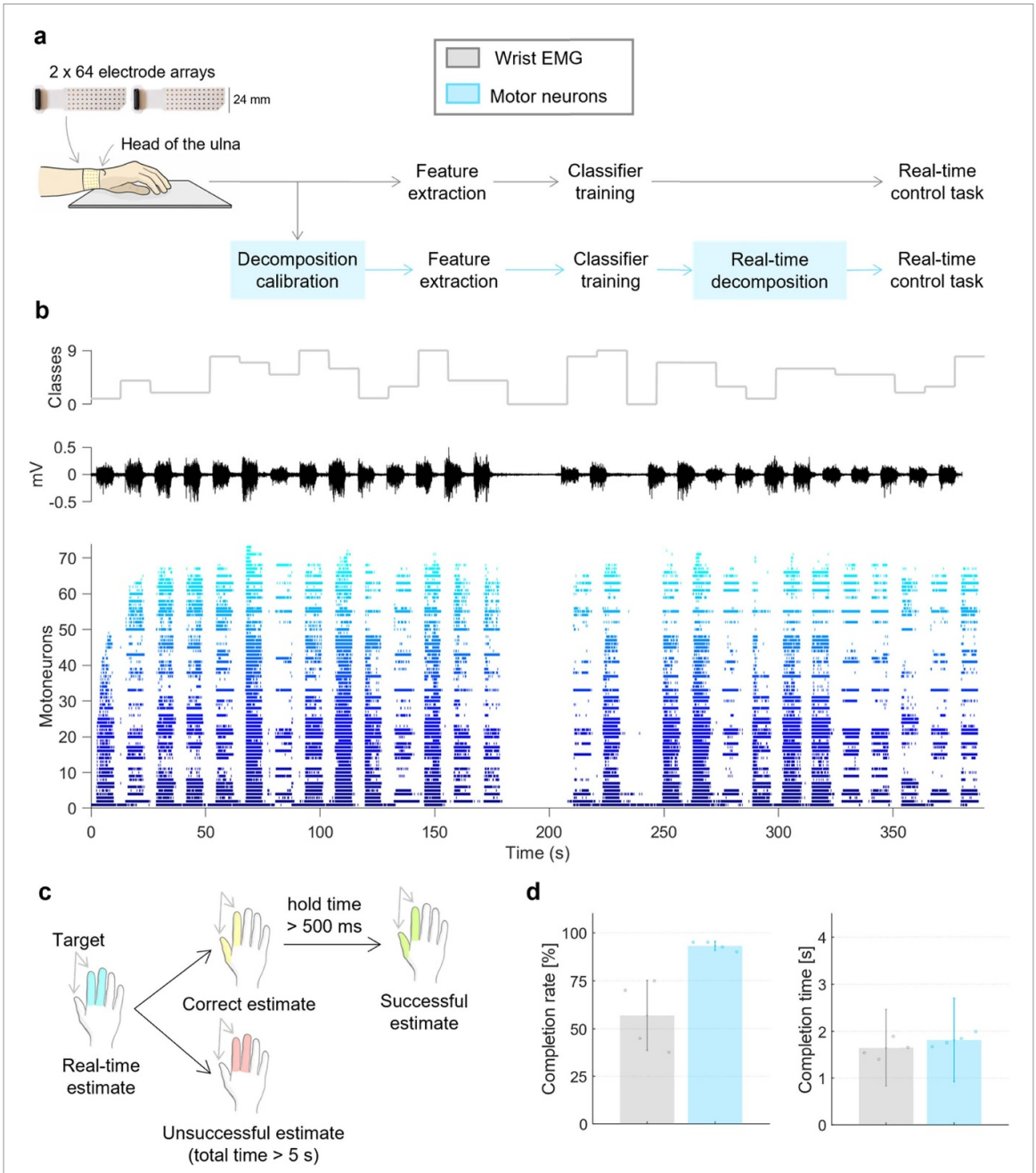


Figure 5. Real-time control. (a) Acquisition setup for the online testing with the processing pipelines for the wrist EMG signals (grey) and decoded motor neurons firings (blue). The additional steps specific of the decomposition algorithm are highlighted in blue. (b) Training set from one representative participant with the class cues on top (each individual finger plus all the combinations of thumb, index, and middle), one wrist EMG signal in the middle, and the decoded motor neuron activity during the decomposition calibration at the bottom. (c) Success and fail conditions for the real-time control task (d) Online control performance for wrist EMG signals (grey) and decoded motor neuron activity (blue) in terms of completion rate and completion time.

potentials generated at the muscle-tendon interface at the wrist. This neural interface provided a high information transfer rate with the accurate real-time control (∼72 ms total delay) of ten commands elicited by finger tasks. Therefore, the presented results are in line with the vision of future portable, battery-operated systems worn at the wrist as unobtrusive and viable neural interfaces to use in daily living.

Each axonal action potential of a motor neuron determines the generation of action potentials in the innervated muscle fibres. Once excited, the muscle fibres undergo depolarisation in a confined portion of their membrane. The depolarisation zone, which has a length of 5–10 mm, propagates along the muscle fibres from the end plate to the tendons. At the tendons, the depolarisation zone extinguishes, generating a so-called far-field potentials. These are non-propagating components produced by the unbalanced dipole moments of the leading and trailing dipoles during their extinction at the muscle-tendon interface. Far-field potentials are short and have temporal high-frequency components that are

less attenuated by the volume conductor than muscle propagating potentials [32]. In theory, differences in muscle fibre conduction velocity, size, position in the volume conductor, and tendon spread would generate unique far-field potentials for each motor neuron enabling their decomposition from EMG signals recorded over tendon regions.

We validated this hypothesis by retracing the far-field potentials to the muscle fibre action potentials from concurrent recordings at the forearm via spike-triggered averaging (figure 3). This approach showed that most of the sources identified at the wrist coincided with action potentials at the forearm muscle fibres which were well above the baseline noise. This result demonstrates the neural origin of the decoded far-field potentials. Indeed, if the decoded activity were not generated by motor neurons, spike-triggered averaging on muscle electrical signals would yield only noise as it would be equivalent to average uncorrelated EMG signals at the forearm. The observation that approximately 30% of the decoded motor neurons did not result in averaged potentials above the noise level is explained by the location of the muscle fibres innervated by the detected motor neurons. For instance, the flexor digitorum superficialis, the flexor digitorum profundus, and the flexor pollicis longus are located deep in the forearm and therefore their innervating motor neurons generate action potentials detectable at the wrist that may not be at the forearm. Interestingly, this indicates that the limitations of EMG recordings to superficial muscles may be surpassed by tendon recordings when multiple muscles converge into a common tendon area, such as at the wrist. In addition to proving the neural origin of the decoded activity by spike-triggered averaging, we also computed the PNR (known estimate of the mean square error [42]), coefficient of variation of the inter spike intervals (associated to the likelihood of erroneously detected action potentials [40]), and action potential discharge rate (used as a physiological indicator [52, 53]). All metrics were well within the expected accuracy and physiological standards, showing that the decoded far-field potentials at the wrist were reliably extracted and corresponded to the neural output from the spinal cord (figure 1).

The number of identified motor neurons (six motor neurons per finger contraction at both force efforts) was consistent with the results by Stachaczyk *et al* [34] who identified between 5 and 8 motor neurons per finger contraction when recording signals from the forearm flexor muscles. Interestingly, however, the PNR levels observed at the wrist in this study were greater than those usually reported for forearm recordings. Moreover, as discussed above, the decoding from the wrist was not biased towards detecting superficial muscles since the effect of the volume conductor at the wrist is less than at the forearm. Furthermore, the signal characteristics at the wrist are different than those at the belly of the muscle. The potentials recorded at the wrist are far-field components [15], which are non-propagating potentials highly synchronised across channels within each motor neuron (as shown in figure 2(d)) and shorter in time than the propagating signals recorded from muscles. These characteristics result in greater temporal sparsity at the tendons because of the shorter duration of the individual potentials. Therefore, the EMG signals recorded over tendons can be modelled as convolutive mixtures in which the filters applied to the sources have relatively short duration. Short duration filters are easier to compensate since they better approximate delta functions that represent the sources. This also results in sparser observations. Overall, we have not only shown that wrist EMG signals can be decoded into the underlying far-field potentials corresponding to motor neuron activity, but also that recording from the wrist may even be preferable over conventional muscle recordings in term of representativeness of the decoded information and accuracy.

From the decoded far-field potentials, we performed an offline classification with the aim of using the wrist interface for control applications. Results showed that the decoded far-field potentials accurately predicted finger tasks for up to ten classes with significantly higher accuracy than that of wrist EMG signals. Still, the classification accuracy of wrist EMG signals (∼83%) was slightly higher than the one obtained by Jiang *et al* [19] in a real-time gesture prediction task (∼75%). Although only four sensors were used in that previous study, their location was consistent with our electrode placement below the head of the ulna. In contrast, Botros *et al* [20] reported higher accuracies (∼88%) for offline single and combined finger prediction using the same feature set, but their electrodes targeted the muscle fibres in the proximal and medial part of the wrist instead of the tendons. The main limitation of the wrist EMG signals is their high crosstalk due to the convergence of the muscle tendons in a reduced space. This contributes to the high overlap between the classes in the spatial activity maps (figure S1 available online at stacks.iop.org/JNE/19/026031/mmedia) and feature space (figure S2) of the tendon electrical signals, which resulted in an overall lower performance than the decoded far-field potentials. In contrast, previous studies by Dai and Hu showed that myoelectric activity spatial maps from the forearm can indeed differentiate between individual finger flexions [55] and extensions [35] when a large muscle area is covered. More notably, myoelectric signals from the entire area of the forearm can separate over 30 finger and wrist gestures in offline conditions when a large dataset is provided (>200 contractions) [56].

To increase the information transfer and enhance the separability between finger classes despite the

limited area, the wrist EMG signals need to be decoded into the neural output of the spinal cord. However, no other study has previously addressed the potential of the wrist for non-invasive neural interfacing, thus the only comparative results are from the forearm. In a finger prediction task, Stachaczyk *et al* [34] obtained similar classification accuracy for the neural output of the spinal cord at the forearm (98%) to the presented here at the wrist (∼97%), although only for individual finger tasks (the four digits, excluding the thumb, while here we tested classification over ten tasks comprising individual and combined finger gestures). Therefore, the reported accuracy in finger task classification when decoding motor neurons from the wrist is even superior to that of motor neurons decoded from muscle tissue. Stachaczyk *et al* [34] also found that the neural output was robust to variations in the force level, unlike myoelectric signals from the forearm when predicting finger flexions [34]. Indeed, the increased classification error of wrist EMG signals when both force levels were combined was in agreement with previous literature on the effect of dynamic contractions in myoelectric pattern recognition [57, 58]. These findings suggest that motor neurons discriminative power between fingers does not rely on spatial information, nor on force encoding. This is supported by the feature map of the decoded wrist EMG signals presented in figure S2 where the different classes exhibit higher separability than in the wrist EMG feature space, despite targeting the same area and corresponding to multiple force levels.

Additional real-time experiments were carried out with multiple repetitions to validate and extend the offline results to real-life interfacing scenarios. This analysis showed that the far-field potentials of the tendon endings at the wrist can be accurately detected and enabled real-time interfacing (∼3 ms) with over 70 motor neurons. Moreover, this neural decoding led to high reproducibility and separability between finger contractions, as evidenced by the high task completion rate (>93%) in relatively short time (∼1.81 s per task). To the best of our knowledge, no other study has previously implemented a pattern recognition approach with neural decoding in real-time.

Nonetheless, these results were obtained during isometric contractions where the position of the arm and hand were fixed. These conditions facilitate the decoding of the motor neuron firings since the decomposition filters are not subjected to the effect of muscle fibre shortening/lengthening, which is typical of dynamic contractions. Yet, this constitutes a highly controlled setup, unlikely to happen in real-life scenarios. Hence, future work should address how these factors affect the robustness and long-term performance of the non-invasive wrist neural interface.

5. Conclusion

In conclusion, we have shown the feasibility of accurate and real-time human-computer interaction from decoded far-field potentials corresponding to motor neuron firings from non-invasive recordings at the wrist. These innovative results open an important perspective in unobtrusive and socially acceptable neural interfaces for general consumer electronics.

Data availability statement

The data that support the findings of this study are available upon reasonable request from the authors.

Acknowledgments

This work was supported by the Engineering and Physical Sciences Research Council—Centre for Doctoral Training in Neurotechnology for Life and Health (I M G), Meta (I M G, D Z W), Academy of Finland—project 'Hi-Fi BiNDIng', No. 333149 (I V), and the European Research Council, Synergy Grant—project Natural BionicS, No. 810346 (D Y B, D F)

Conflict of interest

D Z W is a Research Scientist at Reality Labs with salary and equity compensation from Meta. D F is Scientific Advisor for Reality Labs with compensation for this service from Meta. D Y B and D F are inventors in a patent (Neural Interface. UK Patent Application No. GB1813762.0. 23 August 2018) and patent application (Neural interface. UK Patent Application No. GB2014671.8. 17 September 2020) related to the methods and applications of this work.

Ethical statement

This experimental protocol was approved by the local ethics committee of Imperial College London (reference number 18IC4685) and was conducted in accordance with the Declaration of Helsinki. All participants signed informed consent forms before the experiment.

ORCID iDs

Irene Mendez Guerra https://orcid.org/0000-0001-7361-4618
Deren Y Barsakcioglu https://orcid.org/0000-0002-3115-4577
Ivan Vujaklija https://orcid.org/0000-0002-7394-9474
Dario Farina https://orcid.org/0000-0002-7883-2697

References

[1] Holobar A and Farina D 2021 Noninvasive neural interfacing with wearable muscle sensors: combining convolutive blind source separation methods and deep learning techniques for neural decoding *IEEE Signal Process. Mag.* **38** 103–18

[2] Yuste R *et al* 2017 Four ethical priorities for neurotechnologies and AI *Nature* **551** 159–63

[3] Velliste M, Perel S, Spalding M C, Whitford A S and Schwartz A B 2008 Cortical control of a prosthetic arm for self-feeding *Nature* **453** 1098–101

[4] Deng X, Yu Z L, Lin C, Gu Z and Li Y 2020 A Bayesian shared control approach for wheelchair robot with brain machine interface *IEEE Trans. Neural Syst. Rehabil. Eng.* **28** 328–38

[5] Benabid A L *et al* 2019 An exoskeleton controlled by an epidural wireless brain–machine interface in a tetraplegic patient: a proof-of-concept demonstration *Lancet Neurol.* **18** 1112–22

[6] Moxon K A and Foffani G 2015 Brain-machine interfaces beyond neuroprosthetics *Neuron* **86** 55–67

[7] Shanechi M M 2019 Brain–machine interfaces from motor to mood *Nat. Neurosci.* **22** 1554–64

[8] Martini M L, Oermann E K, Opie N L, Panov F, Oxley T and Yaeger K 2020 Sensor modalities for brain-computer interface technology: a comprehensive literature review *Clin. Neurosurg.* **86** E108–17

[9] Farina D and Aszmann O 2014 Bionic limbs: clinical reality and academic promises *Sci. Transl. Med.* **6** 257–12

[10] Farina D and Negro F 2015 Common synaptic input to motor neurons, motor unit synchronization, and force control *Exercise Sport Sci. Rev.* **43** 23–33

[11] Farina D, Stegeman D F and Merletti R 2016 Biophysics of the generation of EMG signals *Surface Electromyography: Physiology, Engineering and Applications* ed R Merletti and D Farina (Hoboken, NJ: Wiley) pp 1–24

[12] Ahmadizadeh C, Khoshnam M and Menon C 2021 Human machine interfaces in upper-limb prosthesis control: a survey of techniques for preprocessing and processing of biosignals *IEEE Signal Process. Mag.* **38** 12–22

[13] Fang Y-M and Chang C-C 2016 Users' psychological perception and perceived readability of wearable devices for elderly people *Behav. Inf. Technol.* **35** 225–32

[14] Raisamo R, Rakkolainen I, Majaranta P, Salminen K, Rantala J and Farooq A 2019 Human augmentation: past, present and future *Int. J. Hum. Comput. Stud.* **131** 131–43

[15] Dumitru D and Jewett D L 1993 Far-field potentials *Muscle Nerve* **16** 237–54

[16] Stegeman D F, Dumitru D, King J C and Roeleveld K 1997 Near- and far-fields: source characteristic and the conducting medium in neurophysiology *J. Clin. Neurophysiol.* **14** 429–42

[17] Dumitru D and King J C 1991 Far-field potentials in muscle *Muscle & Nerve* **14** 981–9

[18] Jiang X, Merhi L K, Xiao Z G and Menon C 2017 Exploration of force myography and surface electromyography in hand gesture classification *Med. Eng. Phys.* **41** 63–73

[19] Jiang S, Lv B, Guo W, Zhang C, Wang H, Sheng X and Shull P B 2018 Feasibility of wrist-worn, real-time hand, and surface gesture recognition via sEMG and IMU sensing *IEEE Trans. Ind. Inform.* **14** 3376–85

[20] Botros F, Phinyomark A and Scheme E 2020 EMG-based gesture recognition: is it time to change focus from the forearm to the wrist? *IEEE Trans. Ind. Inform.* **18** 174–84

[21] Khushaba R N, Kodagoda S, Takruri M and Dissanayake G 2012 Toward improved control of prosthetic fingers using surface electromyogram (EMG) signals *Expert Syst. Appl.* **39** 10731–8

[22] Cipriani C, Antfolk C, Controzzi M, Lundborg G, Rosen B, Carrozza M C and Sebelius F 2011 Online myoelectric control of a dexterous hand prosthesis by transradial amputees *IEEE Trans. Neural Syst. Rehabil. Eng.* **19** 260–70

[23] Holobar A and Zazula D 2007 Multichannel blind source separation using convolution Kernel compensation *IEEE Trans. Signal Process.* **55** 4487–96

[24] Glaser V, Holobar A and Zazula D 2013 Real-time motor unit identification from high-density surface EMG *IEEE Trans. Neural Syst. Rehabil. Eng.* **21** 949–58

[25] Chen M and Zhou P 2016 A novel framework based on FastICA for high density surface EMG decomposition *IEEE Trans. Neural Syst. Rehabil. Eng.* **24** 117–27

[26] Negro F, Muceli S, Castronovo A M, Holobar A and Farina D 2016 Multi-channel intramuscular and surface EMG decomposition by convolutive blind source separation *J. Neural Eng.* **13** 026027

[27] Barsakcioglu D Y, Bracklein M, Holobar A and Farina D 2020 Control of spinal motoneurons by feedback from a non-invasive real-time interface *IEEE Trans. Biomed. Eng.* **68** 926–35

[28] Farina D, Negro F, Gazzoni M and Enoka R M 2008 Detecting the unique representation of motor-unit action potentials in the surface electromyogram *J. Neurophysiol.* **100** 1223–33

[29] Heckman C J and Enoka R M 2012 Motor Unit *Comprehensive Physiology* vol 2 pp 2629–82

[30] Farina D and Holobar A 2016 Characterization of human motor units from surface EMG decomposition *Proc. IEEE* **104** 353–73

[31] Farina D, Merletti R, Indino B, Nazzaro M and Pozzo M 2002 Surface EMG crosstalk between knee extensor muscles: experimental and model results *Muscle Nerve* **26** 681–95

[32] Dimitrova N A, Dimitrov G V and Nikitin O A 2002 Neither high-pass filtering nor mathematical differentiation of the EMG signals can considerably reduce cross-talk *J. Electromyogr. Kinesiol.* **12** 235–46

[33] Kapelner T, Negro F, Aszmann O C and Farina D 2018 Decoding motor unit activity from forearm muscles: perspectives for myoelectric control *IEEE Trans. Neural Syst. Rehabil. Eng.* **26** 244–51

[34] Stachaczyk M, Farokh Ataszhar S, Dupan S, Vujaklija I and Farina D 2020 Towards universal neural interfaces for daily use: decoding the neural drive to muscles generalises highly accurate finger task identification across humans *IEEE Access* **8** 149025–35

[35] Dai C and Hu X 2020 Finger joint angle estimation based on motoneuron discharge activities *IEEE J. Biomed. Health Inform.* **24** 760–7

[36] Chen C, Yu Y, Ma S, Sheng X, Lin C, Farina D and Zhu X 2020 Hand gesture recognition based on motor unit spike trains decoded from high-density electromyography *Biomed. Signal Process. Control* **55**

[37] Hyvärinen A and Oja E 1997 A fast fixed-point algorithm for independent component analysis *Neural Comput.* **9** 1483–92

[38] Thomas J, Deville Y and Hosseini S 2006 Time-domain fast fixed-point algorithms for convolutive ICA *IEEE Signal Process. Lett.* **13** 228–31

[39] Del Vecchio A, Holobar A, Falla D, Felici F, Enoka R M and Farina D 2020 Tutorial: analysis of motor unit discharge characteristics from high-density surface EMG signals *J. Electromyogr. Kinesiol.* **53** 102426

[40] Holobar A, Minetto M A, Botter A, Negro F and Farina D 2010 Experimental analysis of accuracy in the identification of motor unit spike trains from high-density surface EMG *IEEE Trans. Neural Syst. Rehabil. Eng.* **18** 221–9

[41] Quiroga R Q, Nadasdy Z and Ben-Shaul Y 2004 Unsupervised spike detection and sorting with wavelets and superparamagnetic clustering *Neural Comput.* **16** 1661–87

[42] Holobar A, Minetto M A and Farina D 2014 Accurate identification of motor unit discharge patterns from high-density surface EMG and validation with a novel signal-based performance metric *J. Neural Eng.* **11** 016008

[43] Keenan K G, Farina D, Merletti R and Enoka R M 2006 Amplitude cancellation reduces the size of motor unit potentials averaged from the surface EMG *J. Appl. Physiol.* **100** 1928–37

[44] Del Vecchio A D, Sylos-Labini F, Mondì V, Paolillo P, Ivanenko Y, Lacquaniti F and Farina D 2020 Spinal

motoneurons of the human newborn are highly synchronized during leg movements *Sci. Adv.* **6** eabc3916
[45] Phinyomark A, Phukpattaranont P and Limsakul C 2012 Feature reduction and selection for EMG signal classification *Expert Syst. Appl.* **39** 7420–31
[46] Samuel O W, Asogbon M G, Geng Y, Al-Timemy A H, Pirbhulal S, Ji N, Chen S, Fang P and Li G 2019 Intelligent EMG pattern recognition control method for upper-limb multifunctional prostheses: advances, current challenges, and future prospects *IEEE Access* **7** 10150–65
[47] Ariyanto M, Caesarendra W, Mustaqim K A, Irfan M, Pakpahan J A, Setiawan J D and Winoto A R 2015 Finger movement pattern recognition method using artificial neural network based on electromyography (EMG) sensor *Proc. 2015 Int. Conf. on Automation, Cognitive Science, Optics, Micro Electro-Mechanical System, and Information Technology, ICACOMIT 2015* (IEEE) pp 12–17
[48] Farrell T R and Weir R F 2007 The optimal controller delay for myoelectric prostheses *IEEE Trans. Neural Syst. Rehabil. Eng.* **15** 111–8
[49] Tanzarella S, Muceli S, Del Vecchio A, Casolo A and Farina D 2019 A high-density surface EMG framework for the study of motor neurons controlling the intrinsic and extrinsic muscles of the hand *Proc. Annual Int. Conf. IEEE Engineering in Medicine and Biology Society, EMBS* (*Berlin, Germany*) (IEEE) pp 2307–10
[50] Chen C, Chai G, Guo W, Sheng X, Farina D and Zhu X 2019 Prediction of finger kinematics from discharge timings of motor units: implications for intuitive control of myoelectric prostheses *J. Neural Eng.* **16** 12
[51] Chen C, Ma S, Sheng X, Farina D and Zhu X 2020 Adaptive real-time identification of motor unit discharges from non-stationary high-density surface electromyographic signals *IEEE Trans. Biomed. Eng.* 67 3501–09
[52] Monster A W and Chan H 1977 Isometric force production by motor units of extensor digitorum communis muscle in man *J. Neurophysiol.* **40** 1432–43
[53] Andreassen S and Rosenfalck A 1980 Regulation of the firing pattern of single motor units *J. Neurol. Neurosurg. Psychiatry* **43** 897–906
[54] Enoka R M and Duchateau J 2016 Physiology of muscle activation and force generation *Surface Electromyography: Physiology, Engineering and Applications* 1st edn, ed R Merletti and D Farina (Hoboken, NJ: Wiley) pp 1–29
[55] Dai C and Hu X 2019 Extracting and classifying spatial muscle activation patterns in forearm flexor muscles using high-density electromyogram recordings *Int. J. Neural Syst.* **29** 1850025
[56] Jiang X, Liu X, Fan J, Ye X, Dai C, Clancy E A, Akay M and Chen W 2021 Open access dataset, toolbox and benchmark processing results of high-density surface electromyogram recordings *IEEE Trans. Neural Syst. Rehabil. Eng.* **29** 1035–46
[57] Campbell E, Phinyomark A and Scheme E 2020 Current trends and confounding factors in myoelectric control: limb position and contraction intensity *Sensors* **20** 1613
[58] Phinyomark A, Campbell E and Scheme E 2020 Surface electromyography (EMG) signal processing, classification, and practical considerations *Biomedical Signal Processing* (*Series in BioEngineering*) ed G Naik (Singapore: Springer) pp 3–29